An Analysis of the Large-Signal Characteristics of AlGaAs/GaAs Heterojunction Bipolar Transistors

Michael Y. Frankel, *Student Member, IEEE,* and Dimitris Pavlidis, *Senior Member, IEEE*

Abstract—**The large-signal characteristics of AlGaAs/GaAs heterojunction bipolar transistors are reported. A harmonic balance analysis technique is used for their analysis. This is based on equivalent circuit extractions using approximate physical equations for constraining the fitted solutions and for describing certain circuit element value bias trends. Class A and Class AB large signal behavior was measured and modeled satisfactorily. Power saturation is shown to occur due to the input signal entering the cutoff or the saturation region of the HBT operation. This is illustrated by time-dependent current/voltage waveforms and the power dependence of large-signal equivalent circuit elements. Depending on device bias and matching conditions the main sources of nonlinearities in device output may be caused by the nonlinearities in transconductance, input conductance, and base-collector capacitance.**

I. Introduction

THE SILICON bipolar junction transistor has played a dominant role in the RF power applications from the earliest days of semiconductor electronics [1]. The recent progress in the development of III-V compound semiconductor heterojunction bipolar transistors (HBT) [2]–[5] has necessitated a re-examination of the issues associated with the design of high frequency power devices. Traditionally, the primary power limitation of the bipolar transistors has been attributed to thermal effects [6], [7] as well as to collector junction breakdown [8]. These issues, along with study of third-order distortion and distributed effects have been investigated for BJTs and HBTs [9]–[12]. Also, the transistor thermal limitations have been assessed for the III-V semiconductor bipolar technology theoretically [13], and the output power limitations have been studied experimentally [3], [5].

The inherently strong nonlinearity in the base-emitter voltage to collector current transfer characteristics can detrimentally affect the performance of the device itself or of device matching to the circuit. However, it can also exploited to an advantage for mixer and logarithmic amplifier applications [1], [12]. Modeling of experimental characteristics can help in understanding the large-signal properties of HBT's. Although extensive work has been done in this area for III-V semiconductor field-effect transistors [14]–[16], it is rather limited for HBT's [12], [17].

In the present work an analysis of the HBT behavior is presented under large-signal excitation. A harmonic balance analysis method [18], [19] incorporated into a commercial software package [20] is used for this purpose. It allows device simulation as part of a complete microwave circuit. Additionally, the influence of device intrinsic parameters on circuit operation can be investigated. Section II describes the equivalent circuit model used for nonlinear computations. The model parameters were determined experimentally as described in Section III. In Section IV, the large-signal model is validated by comparing predicted and measured AlGaAs/GaAs HBT power characteristics. Power saturation and HBT nonlinearities are finally analyzed in terms of equivalent circuit elements and time-domain node currents.

II. HBT Equivalent Circuit Model and Parameter Extraction Constraints

The large-signal device analysis procedure used in this work is based on a harmonic balance method and is outlined in Fig. 1. It requires the knowledge of the dc characteristics, two-port bias-dependent ac admittance parameters of the intrinsic device, and charges stored on each node [18]. One method of obtaining these is from the theoretical considerations of the device material and design parameters. An alternate method is to extract the equivalent circuit element values from dc and small-signal *S*-parameter measurements, while conforming with expected physical characteristics. The admittance parameters and stored charges are then obtained from the equivalent circuit. The latter method was used in this work and its application to specific HBT structures is explained in Section III. The model used in this Section was used in order to explore the large-signal behavior of experimentally characterized AlGaAs/GaAs HBTs.

The dc characteristics of the device are modeled with conventional Ebers-Moll-type equations with parameters obtained from fitting to dc measurements. [24] The small-signal ac HBT characteristics were modeled using the equivalent circuit of Fig. 2. Similar to results of Nelson *et al.*, [21], we have found the hybrid-π topology to produce a better fit to *S*-parameter data. It should be noted,

Manuscript received October 23, 1990; revised October 1, 1991. This work was supported by the Air Force Office of Scientific Research, University Research Initiative (Contract F49620-87-C-0016), Alcatel-Espace (Contract 393 500 143), and the Army Research Office (Contract DAAL-03-87-K-0007).

M. Frankel was with the Department of Electrical Engineering and Computer Science, 2238 EECS Building, University of Michigan, Ann Arbor, MI 48109-2964. He is now with the Naval Research Laboratory, Optical Sciences Division, CODE 6570, Washington, DC 20375-5000.

D. Pavlidis is with the Department of Electrical Engineering, and Computer Science, 2228 EECS Building, University of Michigan, Ann Arbor, MI 48109-2964.

IEEE Log Number 9105450.

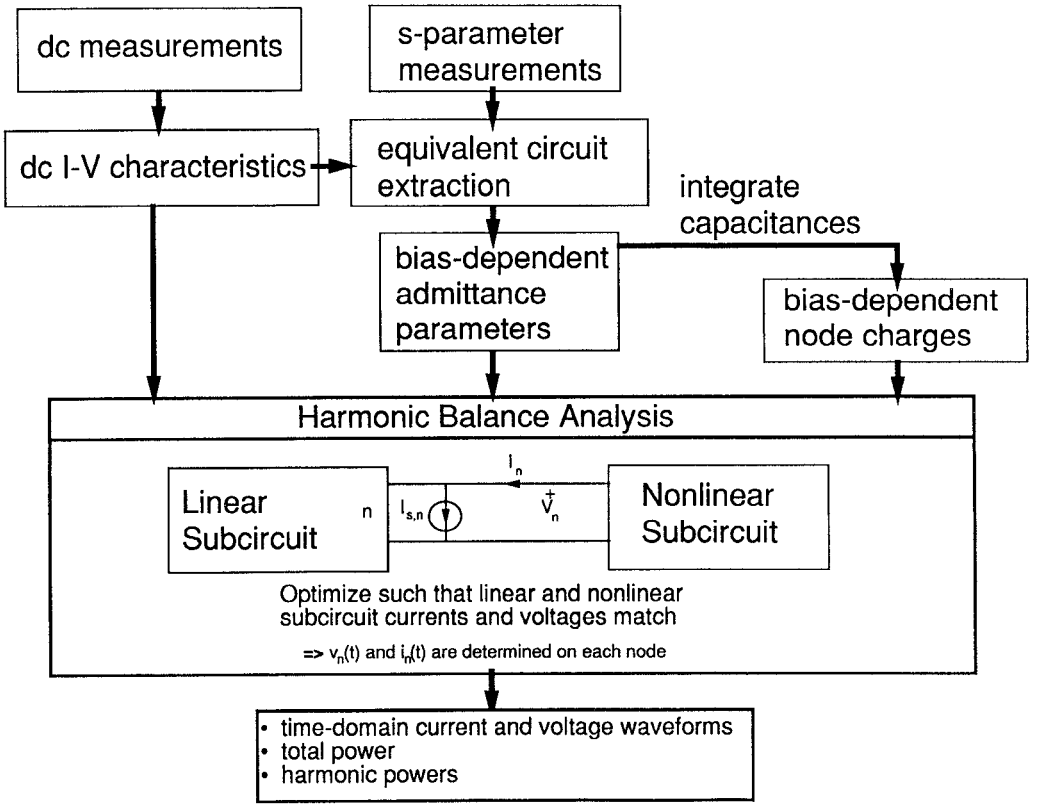

Fig. 1. Large-signal HBT harmonic balance-based analysis procedure.

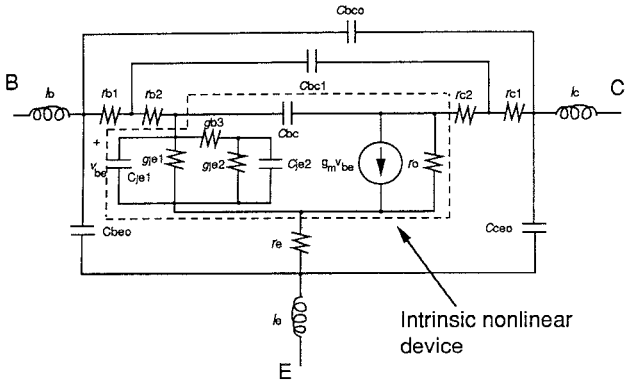

Fig. 2. Small-signal equivalent circuit with distributed-base elements.

however, that of primary interest for this analysis are the admittance parameters and charges only; these can be obtained through network analysis from any equivalent circuit topology. The intrinsic device elements are shown within the dashed outline of Fig. 2. The distributed nature of the base-emitter junction is taken into account by incorporating the additional junction access conductance g_{b3} and the junction conductance and capacitance terms g_{je2} and c_{je2} respectively. This improves the fit between the modeled and the measured input impedances at high frequencies for one of the tested devices (HBT-A). Only the intrinsic elements were assumed to be bias dependent. A number of bias independent elements have been added to the model to account for extrinsic parasitics.

Some physical considerations were made in examining the bias dependence of the intrinsic-device circuit elements (see Fig. 2). This allowed both to verify the equivalent circuit extraction procedure, as well as to give some indication of the physical processes involved in HBT operation. Although different quantitatively, the qualitative character of HBT operation is similar to that of Si BJT's [22]. Simplified analytical expressions applicable to Si bipolar transistors [23], [24] were employed for this reason in order to restrain the number of possible solutions in fitting the HBT equivalent circuit parameters to S-parameter measurements. Analytical expressions of this type may also be used to simplify the description of the bias dependence of a number of equivalent circuit elements. This makes the computations much more efficient while maintaining sufficient accuracy. The way that these relations are used in establishing the HBT small-signal equivalent circuit, as well as describing the bias dependence, is outlined in Section III.

The nature of the minority charge injection into the base imposes an exponential dependence of the base current I_b and the collector current I_c on the applied base-emitter voltage V_{be} in the forward active biasing region as

$$I_b = I_{\text{bo}}\left(\exp\frac{V_{\text{be}}}{n_b V_t} - 1\right) + I_{\text{br}}\left(\exp\frac{V_{\text{be}}}{n_r V_t} - 1\right). \quad \text{(1a)}$$

$$I_c = \beta I_b. \quad \text{(1b)}$$

The symbols used in the equations in this paper are defined in the nomenclature at the end of the paper. Although β can vary in HBTs in a different manner than in

homojunction devices, it was at first approximation considered constant with I_b following our experimental characterizations. As shown later, these reflected an almost constant $\beta - I_b$ relation over the measurement range.

When the device is biased above the recombination-dominated region, the transconductance can be expressed as

$$g_m = \frac{I_c}{n_c V_t}, \tag{2}$$

and the input base-emitter conductance component is

$$g_{je} = \frac{I_b}{n_b V_t}. \tag{3}$$

The total input base-emitter capacitance c_{je} includes the base-emitter depletion capacitance c_{te} and the diffusion capacitance c_{de} associated with the charge carrier storage in the base. The depletion capacitance, c_{te}, can be derived in a manner similar to conventional junction depletion capacitance including the effect of the dielectric permittivity change due to Al composition grading in the emitter [25]. It is approximately independent of current due to both a weak base-emitter voltage dependence and the logarithmic dependence of the voltage on current. The diffusion capacitance, however, does depend on current and is given by

$$c_{de} = \tau_f g_m, \tag{4}$$

where τ_f is the forward carrier transport time. This approximation is valid for our frequency range of interest since τ_f is much shorter (of the order of 1–2 ps for the tested HBT's) than the input signal period (typically over 50 ps in the frequency range of interest which does not exceed 16 GHz). The true c_{de} behavior may not, however, follow very closely this expression at higher operating frequencies. Combining (1b), (2), and (4), the total base-emitter capacitance c_{je} is

$$c_{je} = c_{te} + \frac{\tau_f \beta I_b}{n_c V_t}, \tag{5}$$

The feedback capacitance c_{bc} also includes two effects. There is a contribution due to the charge modulation resulting from the base-collector-voltage-induced basewidth modulation—the Early effect. This portion of the c_{bc} is negligible due to the high base doping and correspondingly insignificant basewidth modulation. The dominant capacitance is due to the base-collector depletion region and follows a conventional depletion region capacitance formula [24, p. 190].

The base-collector conductance g_{bc} is negligible due to the insignificant basewidth modulation and the resulting high Early voltage V_a as reflected by

$$g_{bc} = \frac{V_t}{|V_a|} \frac{g_m}{\beta}. \tag{6}$$

Finally, the output conductance $g_o = 1/r_o$ is also negligible as

$$g_o = \frac{V_t}{|V_a|} g_m. \tag{7}$$

III. DC and Microwave Characterization and Modeling

Two different AlGaAs/GaAs HBTs were investigated. The base had no compositional grading and its thickness was 1000 Å. In addition to design and fabrication differences, the first one (HBT-A) had eight and the second (HBT-B) had four 2 × 30-μm emitter fingers. The operating limits of the devices, as well as estimates of the optimal operating points, were obtained from the measured I_c versus V_{ce} characteristics with I_b as the parameter (see Fig. 3 for HBT-B). From the $I_c - V_{ce}$ characteristics, $\beta = I_c/I_b$ (1b) can be determined and are shown in Fig. 4. HBT-A delivers approximately twice the current of HBT-B with a maximum operating current $I_c \approx 70$ mA at $I_b \approx 30$ mA versus $I_c \approx 40$ mA at $I_b \approx 3$ mA. Further, five distinct regions of the device operation can be identified, as shown on Fig. 3 for an AlGaAs/GaAs HBT-B. The first and second regions indicate device active and cutoff bias conditions, respectively. It is these regions that are of the most interest for device operation. The third region indicates saturation biasing and is generally avoided in microwave circuits. Biasing the device into the fourth region, which is shown only schematically in the figure, results in the base-collector junction breakdown. The fifth region is characterized by a rapid degradation of β.

In Si BJT's the β degradation is related to the base pushout (Kirk effect). An effect of this type is less likely in HBTs than in Si BJT's at the current densities used (typically below $5 \cdot 10^4$ A/cm^2) due to the high HBT base doping and velocity overshoot effects in the collector [22]. The current gain degradation observed in the fifth region for tested HBTs seems to be primarily attributed to thermal effects. This was supported by the strong dependence of the degradation limits on the type of mounting. Furthermore, the degradation was more severe at low I_c high V_{ce} bias points, which is consistent with silicon bipolar transistor thermal breakdown models, but refutes push-out.

As mentioned already, base push-out was ruled out as a possible mechanism in the fifth region due to the low current densities at which gain degradation was initiated. An additional reason for ruling out base push-out comes from the fact that decreasing power dissipation allowed an increase of both I_c and I_b without any significant loss of β. This is the opposite of what one would expect in the presence of base push-out. Finally, collector-base junction breakdown was ruled out since no significant current increases were observed at higher V_{ce}, as long as the measurement range was limited to 5 V.

The active and the cutoff regions of the device operation are of primary importance for microwave circuits.

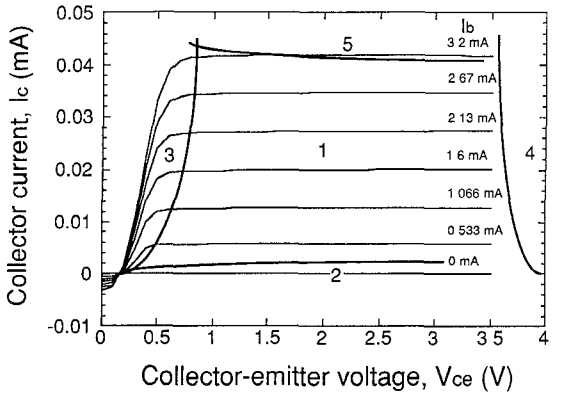

Fig. 3. HBT-B $I_c - V_{ce}$ characteristics.

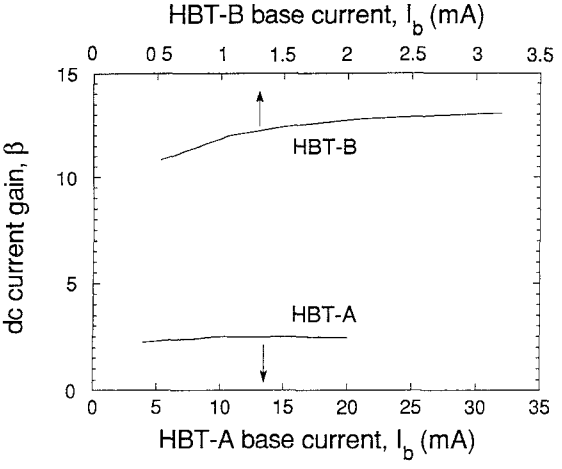

Fig. 4. dc current gain β in forward active region (V_{ce} = 2.7 V).

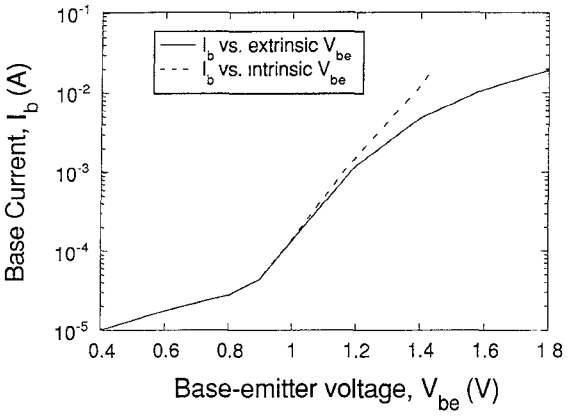

Fig. 5. Gummel plot of I_c versus extrinsic and intrinsic V_{be} for HBT-A.

These regions are also associated with maximum efficiency of operation. Thus, a large number of experimental data were collected when characterizing the HBT's in these two regions. This ensures accurate modeling in the regions of interest. Since the device can enter the saturation region during large-signal ac operation, the Ebers–Moll model used for dc characteristics was defined for cutoff, forward active, and saturation regions.

The dc current gain β, shown in Fig. 4 for both devices at $V_{ce} \approx 2.7$ V, was evaluated from (1b) where I_c and I_b are obtained from dc $I_c - V_{ce}$, I_b characteristics, shown in Fig. 3. As can be seen, β is approximately constant for both devices in the active region where the equivalent circuit was extracted. The $n_b V_t$-product (see (1a)) was determined from the slope of the Gummel plot (Fig. 5 for HBT-A) above the low-current recombination region ($4 \cdot 10^5$ A) and below the high-current region (10^3 A).

The high frequency characteristics of the HBT were determined by S-parameter measurements at various bias points, particularly concentrated in the forward active region. The elements of the equivalent circuit shown in Fig. 2 were then derived at each bias point by fitting calculated to measured S-parameters using the gradient optimizer of Libra. The extrinsic parasitic elements were verified to be substantially independent of the bias, as expected. The equivalent-circuit intrinsic-element variation with V_{ce} was insignificant for HBT-A, but was present for HBT-B. In the active region of both HBT's, the intrinsic device parameters were strong functions of I_b. A large number of possible solutions is obtained for the equivalent circuit if no constraint is imposed during optimization. To obtain some consistency in the equivalent circuit results, as necessary for the analysis of the large-signal HBT properties, some constraints were imposed on the ac transconductance g_m, which was limited to lie within 20% of its dc value. The other parameters were only loosely constrained.

Following the above procedure, the extrinsic base and emitter access resistances obtained from the microwave equivalent circuit extraction proved to be close to their dc values. These ac values could in fact be used to account for the difference in dc intrinsic and extrinsic base-emitter voltages. Fig. 5 shows, for example, the HBT-A Gummel plot of I_b as a function of extrinsic (_____ dc measured) and intrinsic (----estimated from dc measurements using ac r_{b1}, r_{b2}, and r_c values) base-emitter voltage. The results indicate a level of consistency between the small-signal ac and dc measurements and models.

Fig. 6(a)–(c) show the base-emitter conductances (g_{je1}, g_{je2}, g_{b3}) and capacitances (c_{je1}, c_{je2}) extracted using the above described g_m constraint as functions of I_b for HBT-A. In Fig 6(a) and (b), the dashed lines (----) are third-order polynomial fits to extracted equivalent circuit elements. The solid lines (_____) are fits of (3) and (5) to the extracted elements. As will be shown in Section VI, these can be used instead of the polynomial fits in order to improve the efficiency of the large-signal computation, while maintaining enough modeling accuracy. Since β is constant, the I_b dependence of g_{je1}, g_{je2}, c_{je1}, c_{je2} (see Figs. 6(a)–(b)) is linear. The conductance variation in Fig. 6(a) (_____) follows (3) with the fitted $n_b V_t$-product of 0.065 V. This ac determined value compares well to 0.073 V obtained from the dc measurements. From the capacitance data in Fig. 6(b) and the approximate fitted results using (5) (solid line), one determines $\tau_f \approx 1.35$ ps. Therefore, τ_f is indeed much shorter than input signal period (>50 ps), supporting the assumption made in (4) (see dis-

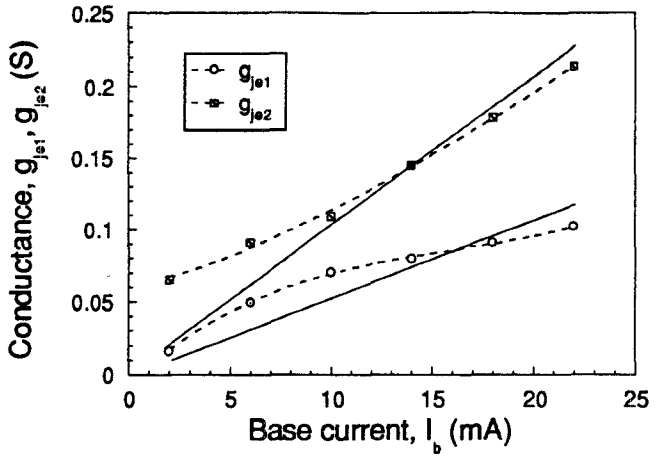

(a)

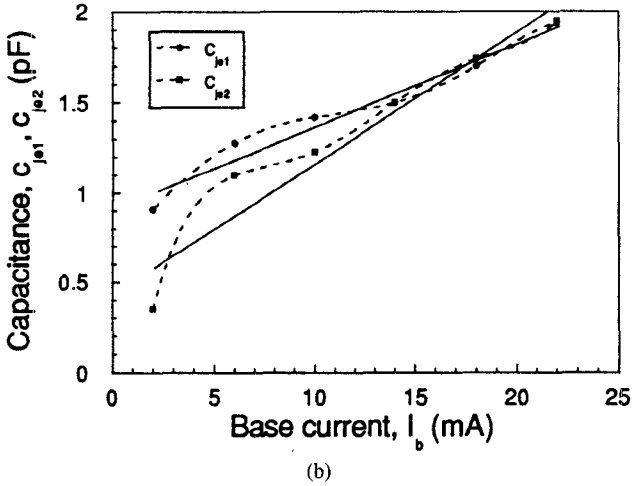

(b)

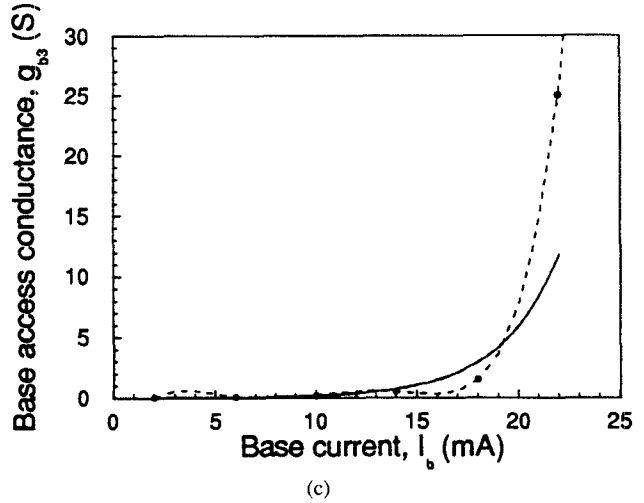

(c)

Fig. 6. (a) HBT-A base-emitter (input) conductances; (b) HBT-A base-emitter (input) capacitances; and (c) HBT-A base access conductance as extracted from *S*-parameter measurements by equivalent circuit fitting. Solid lines show fitting to the measured data used in the large-signal model.

cussion in Section II). The conductance g_{b3} in Fig. 6(c) models the distributed effects in the base; its behavior is difficult to predict analytically and an exponential fit is used in this case. It is interesting to note that the current-crowding effect at higher current levels reduces the distributed nature of the base, thereby increasing the observed conductance along it. Finally, the g_{bc} and g_o values extracted from the equivalent circuits proved to be negligibly small (below $10^{-6}(S)$). This justifies the comments made in Section II regarding their negligible impact on the active characteristics of the device.

TABLE I
HBT-A BIAS-INDEPENDENT EQUIVALENT CIRCUIT ELEMENT VALUES AND FUNCTIONAL FITS USED FOR BIAS-DEPENDENT ELEMENTS

Bias Independent HBT-A Parameters					
l_c	0.03 nH	c_{bco}	$20\ 10^{-5}$ pF	r_e	7.65 Ω
l_b	0.003 nH	r_{b1}	0.013 Ω	c_{bc}	0.25 pF
l_e	0.03 nH	r_{b2}	0.41 Ω		
c_{beo}	0.17 pF	r_{c1}	2.9 Ω		
c_{ceo}	0.13 pF	r_{c2}	8.9 Ω		
c_{bc1}	$4.2\ 10^{-5}$ pF	r_o	$5\ 10^{7}$ Ω		

Bias Dependent HBT-A Parameters	
$g_m = 34\ I_b$(S)	$g_{b3} = 0.0062\ e^{(34.3\ 4\ I_b)}$(S)
$g_{je1} = 5.3\ I_b$(S)	$c_{je1} = 0.9 + 46\ I_b$(pF)
$g_{je2} = 10.2\ I_b$(S)	$c_{je2} = 0.44 + 73\ I_b$(pF)

Table I summarizes the HBT-A bias-independent equivalent-circuit-element values as obtained through *S*-parameter fitting. It also gives the functions, valid in the active region, used to describe the bias dependent elements in the large-signal model. These were obtained using (2) for g_m and (3) and (5) for g_{je} and c_{je} as described above.

Figs. 7(a)-(c) show the base-emitter conductance g_{je}, the base-emitter capacitance c_{je}, and the base-collector capacitance c_{bc} as functions of both I_b and V_{ce} for HBT-B. These results were fitted by analytic functions for the purpose of modeling their bias dependence. In general, one sees a similar parameter dependence on I_b in the active region as for the previous HBT-A. The dc current gain β is constant in the active region where the equivalent circuit is extracted. The base-emitter conductance and base-emitter capacitance show a linear dependence on I_b in the active region. A weak dependence on V_{ce} is also seen. In the active region the base-collector capacitance c_{bc} shows only a weak dependence on I_b and V_{ce}. However, one sees a rapid increase in the base-collector capacitance at lowest V_{ce} due to the HBT-B beginning to enter the saturation region where a corresponding base-charge increase takes place. Simple functions summarized in Table II were used to describe these bias-dependent elements. Table II specifies also as in the case of HBT-A the extrinsic bias-independent element values.

IV. LARGE-SIGNAL POWER CHARACTERISTICS AND ANALYSIS

The system used to measure device output versus input power characteristics is capable of operation from 0.5 to 18 GHz. Class A (V_{ce} = 3 V, I_b = 15 mA) and Class AB (V_{ce} = 3 V, I_b = 5 mA) dc biases were used for HBT-A. The device was operated outside the high-current region where a thermal (see Section III) degradation of I_c and β

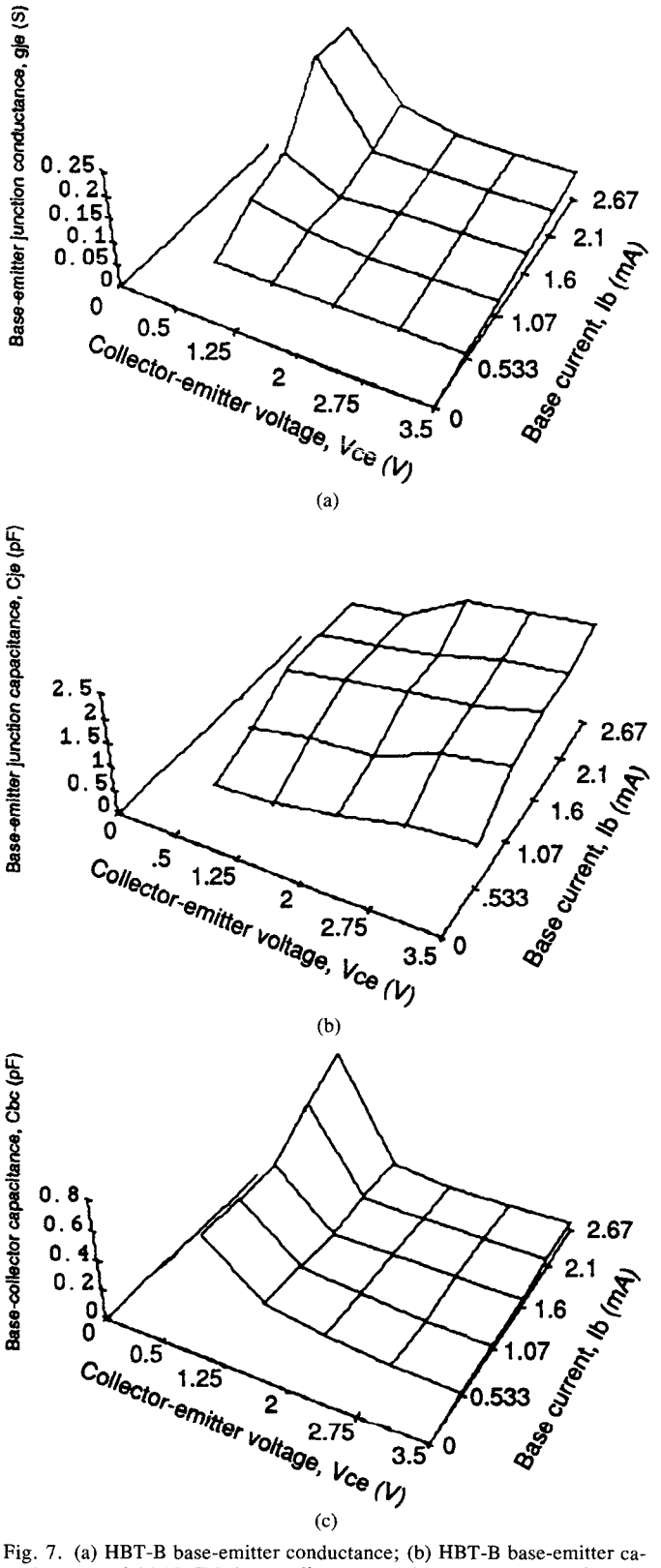

Fig. 7. (a) HBT-B base-emitter conductance; (b) HBT-B base-emitter capacitance; and (c) HBT-B base-collector capacitance as extracted from *S*-parameter measurements by equivalent circuit fitting.

occurs. The devices had a maximum frequency of oscillation $f_{max} \approx 12$ GHz and the short-circuit-gain cutoff frequency, $f_t \approx 20$ GHz. The operating frequency for the large-signal tests was 5 GHz; this allowed two harmonics to fit within the passband of both the device and the measurement system.

TABLE II
HBT-B BIAS-INDEPENDENT EQUIVALENT CIRCUIT ELEMENT VALUES AND FUNCTIONAL FITS USED FOR BIAS-DEPENDENT ELEMENTS

Bias Independent HBT-B Parameters					
l_c	0.03 nH	c_{bco}	0.29 pF	r_e	0.1 Ω
l_b	0.415 nH	r_{b1}	8.8 Ω		
l_e	0.01 nH	r_{b2}	0.0055 Ω		
c_{beo}	0.63 pF	r_{c1}	14.2 Ω		
c_{ceo}	0.02 pF	r_{c2}	12.2 Ω		
c_{bc1}	0.012 pF	r_o	10^7 Ω		

Bias Dependent HBT-B Parameters	
$g_m = 30.3\ I_b$(S)	$c_{je} = 500\ I_b C_{ce}$(pF)
$g_{je} = 28.4\ I_b$(S)	$c_{bc} = 1/(1 + 6.816\ V_{ce})$ (pF)

A harmonic balance method was used to calculate the device power output and gain characteristics as a function of input power. The harmonic balance method solves the nonlinear portion of the circuit in the time-domain. Thus, time-domain voltage and current waveforms for each input power are directly available. Four harmonics were included in the calculations; a larger number did not result in any significant improvement in the accuracy of predicting the experimental behavior. The bias dependent equations of Table I were implemented in Libra as a user-defined element of the intrinsic device model. The parasitics were included as external elements, assumed to be bias independent (see also Table I). Fig. 8 shows the agreement between the measured and the calculated power and gain characteristics in both Class A and Class AB operation for HBT-A. Under 50-Ω terminating conditions the power-gain difference between Class A and Class AB operation is enhanced due to the 50 Ω loads used in the experiment. No saturation takes place in Class A operation at the investigated input power levels. The intrinsic device nonlinearities do not consequently cause power saturation in this case where the device operation is limited only to the active region.

However, in Class AB operation the transistor shows output power saturation. Calculated collector current waveforms as a function of input power are shown in Fig. 9 for Class AB operation. From these waveforms we can see that power saturation can be directly attributed to the device entering the cutoff region. This is reflected by the lower half of the current waveform which begins to clip and is accompanied by the decrease of the available output power. The influence of intrinsic device nonlinearities on the overall power characteristics of Class AB operation is small. This can be seen in Fig. 10, which shows the three lowest harmonics are at least 10 dB below the fundamental.

The importance of accurate modeling of the bias-dependent equivalent circuit elements becomes apparent when the device is matched at both the input and output. Load-pull measurements have been performed on HBT-B at 8 GHz. Electromechanical tuners (Focus Inc.) were

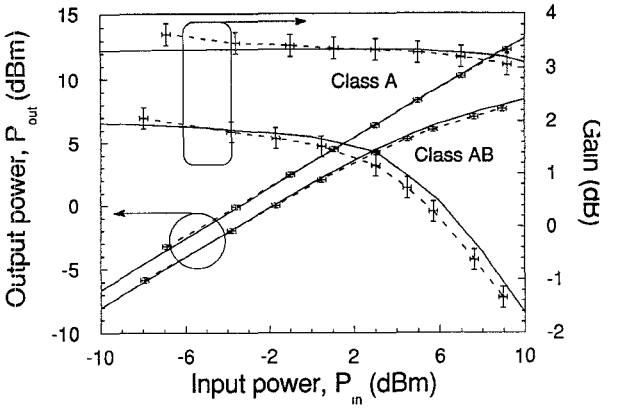

Fig. 8. Output power and gain for HBT-A Class A and Class AB bias cases with 50 Ω terminations (---- measured, —— modeled).

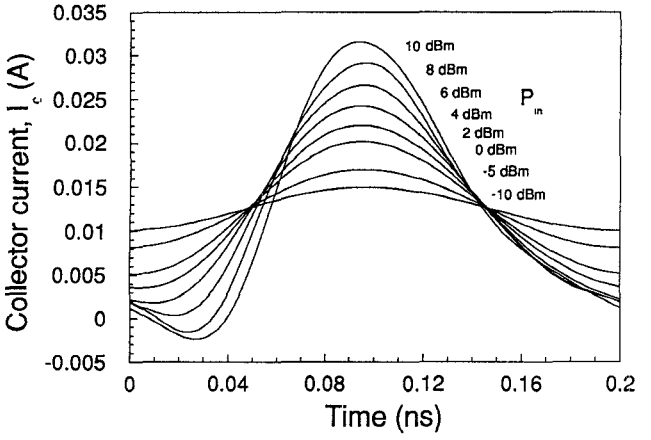

Fig. 9. Class AB simulated collector current waveforms with P_{in} as parameter.

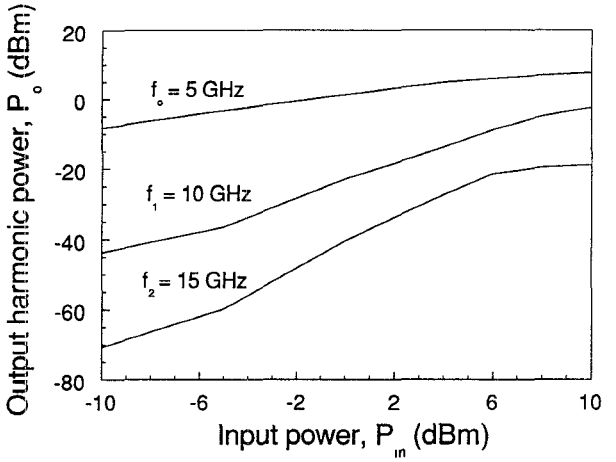

Fig. 10. Simulated Class AB three lowest output power harmonics.

used to provide input and output terminating impedances with values close to simultaneously conjugately matched conditions. For this measurement, the device was biased into a Class A operation (V_{ce} = 2.73 V, I_b = 2.13 mA). Fig. 11 shows the comparison between the modeled and the measured power and gain characteristics. Unlike previous Class A results (shown in Fig. 8 for HBT-A), HBT-

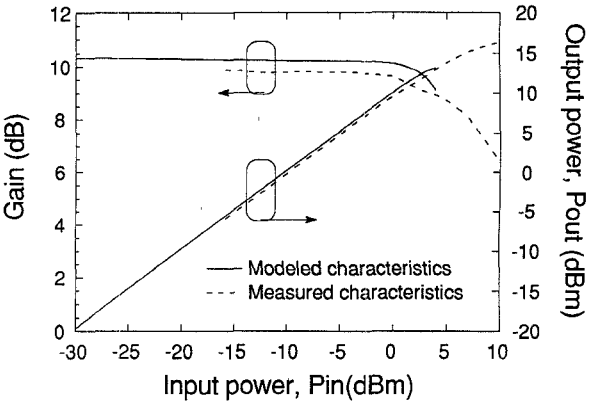

Fig. 11. Output power and gain for HBT-B Class A bias case with matched terminations.

B shows saturation within the same range of input power levels; as discussed earlier HBT-B had half the number of emitter fingers as HBT-A. The analysis of the HBT nodal voltages and currents revealed that the power saturation of HBT-B is a direct result of the device entering the saturation region for a portion of its operating cycle. The discrepancy between the modeled and the measured results is attributed to the inaccuracies in modeling the bias-dependent elements. The results for the simultaneously conjugately matched condition are more sensitive to the equivalent circuit parameter inaccuracies than are those for an unmatched condition.

The large-signal HBT behavior can be further analyzed by defining equivalent large-signal circuit elements, as has been done for FETs [26]. These can be used to calculate power dependent large-signal S-parameters and matching conditions. The large-signal transconductance at the fundamental frequency can be defined as

$$G_m = \left| \frac{F\{I_{gm}(t)\}}{F\{V_{be}(t)\}} \right|_{\omega_o}, \tag{8}$$

where $F\{\}$ denotes a Fourier transform. The large-signal current through this element is

$$I_{gm}(t) = \int_t g_m(t) \frac{dV_{be}(t)}{dt}\, dt, \tag{9}$$

and $V_{be}(t)$ is obtained from time-domain harmonic balance calculations.

Similarly, calculating the base-emitter large-signal current as

$$I_{je}(t) = c_{je}(t) \frac{dV_{be}(t)}{dt} + \int_t g_{je}(t) \frac{dV_{be}(t)}{dt}\, dt, \tag{10}$$

we can define the large-signal input conductance as

$$G_{je} = \mathrm{Re}\left\{ \frac{F\{I_{je}(t)\}}{F\{V_{be}(t)\}} \right\}_{\omega_o}, \tag{11}$$

the large-signal input capacitance as

$$C_{je} = \frac{1}{\omega_o} \mathrm{Im}\left\{ \frac{F\{I_{je}(t)\}}{F\{V_{be}(t)\}} \right\}_{\omega_o}, \tag{12}$$

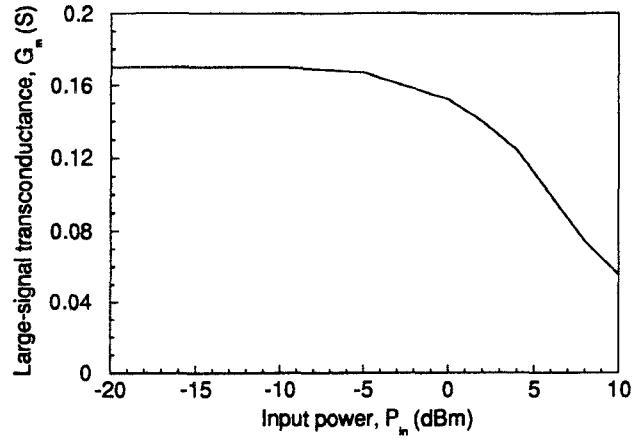

(a)

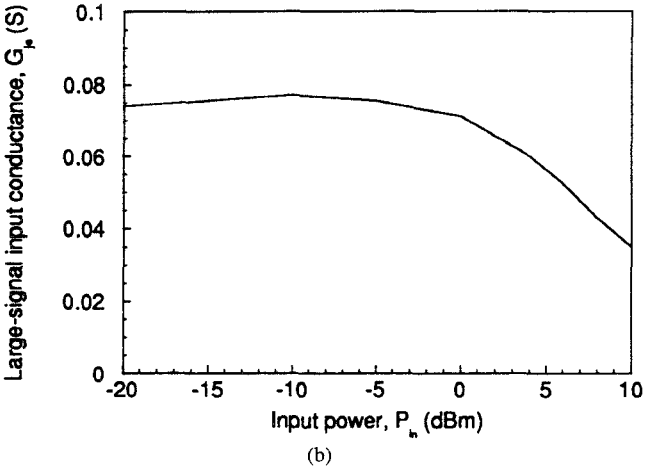

(b)

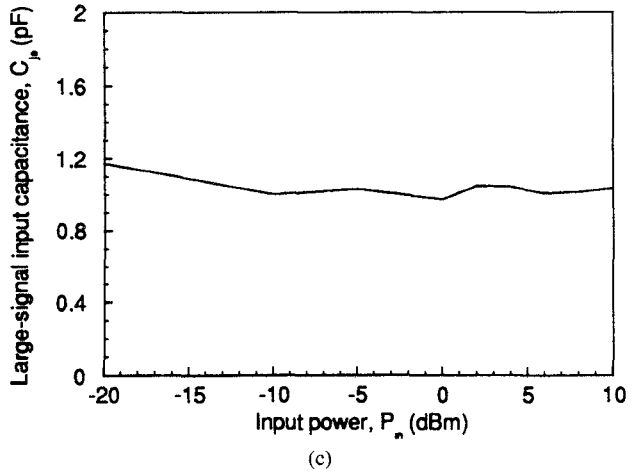

(c)

Fig. 12. HBT-A Class AB equivalent large-signal elements. (a) G_m; (b) G_{je}; (c) C_{je}.

and the large-signal base-collector capacitance as

$$C_{bc} = \frac{1}{\omega_o} \operatorname{Im} \left\{ \frac{F\{I_{bc}(t)\}}{F\{V_{bc}(t)\}} \right\}_{\omega_o}. \tag{13}$$

Fig 12(a)–(c) show the large-signal equivalent circuit elements as functions of the input power calculated from (8)–(12) for the HBT-A Class AB bias case. These results were obtained using the fitted physical equations (3), (5).

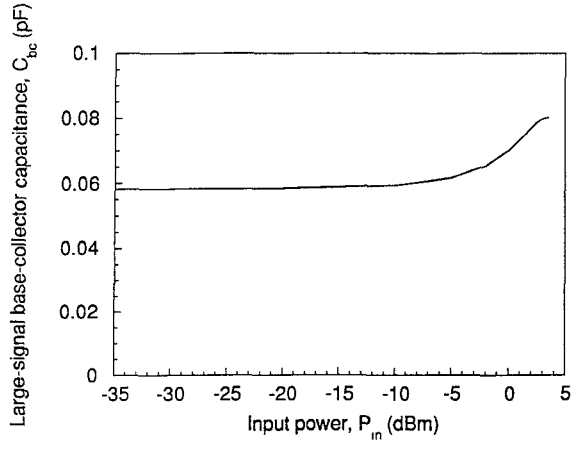

Fig. 13. HBT-B Large-signal base-collector capacitance C_{bc}.

Calculations were also performed using polynomial fits to the input conductances g_{je1}, g_{je2} and input capacitances c_{je1} and c_{je2}. The difference between the results obtained by the two approaches is marginal, in this case suggesting the validity of the physical fitting approach. The large-signal transconductance G_m of Fig. 12(a) follows the gain versus input power characteristics quite closely. It is fairly constant in the linear power region, but drops off rapidly when the device operation begins to enter the cutoff region. Equations (1b), (2), and (3) suggest that the small-signal input conductance trends with input power are similar to the transconductance ones. This is indeed the case, as shown in Fig. 12(b), where the large-signal behavior of the input conductance G_{je} is found to exhibit a rapid decrease with high input powers. The large-signal input capacitance C_{je} (Fig. 12(c)), on the other hand, is constant throughout the whole input power range. This may be attributed to only a weak dependence of the small-input capacitance C_{je} on the device bias. Similarly, the large-signal base-collector capacitance C_{bc} is constant.

Similar quantities were calculated for a HBT-A Class A bias case. However, the large-signal element values deviate little from the small-signal ones as the device never enters saturation under the measurement conditions of the experiments. This fact serves to confirm that the device nonlinearities do not significantly compromise the saturation of the output power.

The large-signal elements for the case of the matched HBT-B in Class A are similar to those of HBT-A in Class AB, with one important exception regarding base-collector capacitance C_{bc}. This large-signal value of C_{bc} was determined by (13) and is shown in Fig. 13. The C_{bc} shows a rapid increase at input powers exceeding -5 dBm where the HBT-B output power begins to saturate. This increase is due to the forward-biasing of the base-collector junction which causes increased base charge storage during a portion of the device operating cycle. The further supports the conclusion that the device power saturation can be attributed in this case to device operation entering the saturation region.

V. Conclusion

The large-signal characteristics of AlGaAs/GaAs HBT's were investigated. Equivalent circuits were extracted for this purpose from measured small-signal S-parameters by fitting. To enhance the physical significance of the equivalent circuits, fitting was constrained by using dc determined transconductance values. Bias dependent equations were then obtained for the equivalent circuit elements by employing approximate HBT physical equations. This provides some physical significance in the analysis of the large-signal characteristics and allows more efficient calculations, which were performed using a harmonic-balance simulator. Reasonable agreement was obtained between computed power and gain versus input power characteristics and directly measured results. The power-saturation mechanisms have been investigated with the help of time current/voltage waveforms and power-dependent equivalent circuit elements. Saturation has been shown to be due to device entering the cutoff or saturation regions of operation depending on class of operation, matching conditions, and power levels used.

Nomenclature

Note: All small signal symbols are lower case and all large-signal or dc symbols are upper case.

β	dc current gain.
C_{bc}	Large-signal base-collector capacitance.
c_{bc}	Base-collector capacitance
c_{de}	Diffusion component of input base-emitter capacitance.
C_{je}	Large-signal input base-emitter capacitance.
$c_{je1,2}$	Input base-emitter junction capacitance.
c_{te}	Depletion component of input base-emitter capacitance.
f_{max}	Maximum frequency of oscillation.
f_t	Current gain cutoff frequency.
g_{b3}	Distributed base-emitter junction access conductance.
g_{bc}	Base-collector conductance.
G_{je}	Large-signal input base-emitter conductance.
$g_{je1,2}$	Input base-emitter junction conductances.
G_m	Large-signal transconductance.
g_m	Transconductance.
$g_o = 1/r_o$	Output conductance.
I_b	Base dc current.
$I_{bc}(t)$	Time-dependent base-collector current.
I_{bo}	Base saturation current.
I_{br}	Base recombination saturation current.
I_c	Collector dc current.
$I_{gm}(t)$	Current through the transconductance element.
$I_{je}(t)$	Time-dependent base-emitter current.
n_b	Base current ideality factor.
n_c	Collector current ideality factor.
n_r	Recombination-dominated region base current ideality factor.
$r_{b1,2}$	Base lead resistance.
r_e	Emitter lead resistance.
$r_o = 1/g_o$	Output resistance.
τ_f	Forward carrier transport time.
V_a	Early voltage.
$V_{bc}(t)$	Time-dependent intrinsic base-collector voltage.
V_{be}	Intrinsic base-emitter voltage.
$V_{be}(t)$	Time-dependent intrinsic base-emitter voltage.
V_{ce}	Collector-emitter voltage.
$V_t = kT/q$	Thermal voltage.
ω_o	Fundamental input signal frequency.

Acknowledgment

The authors would like to acknowledge Dr. B. Bayraktaroglu from Texas Instruments for providing the HBT's used in the tests. The authors would also like to acknowledge the help of M. Tutt in setting up the network analyzer measurements and Y. Kwon for suggesting the use of the distributed base-emitter junction model. One of the authors (MYF) wishes to thank Siemens, Munich for financial support and Prof. G. A. Mourou for encouragement and support.

References

[1] H. O. Granberg, "FETs versus BJTs: making the proper choice for RF power," *Microwaves & RF*, pp. 125–135, Aug. 1989.

[2] B. Bayraktaroglu, N. Camilleri, H. D. Shih, and H Q. Tserng, "AlGaAs/GaAs heterojunction bipolar transistors with 4W/mm power density at X-band," in *1987 IEEE MTT-S Int. Microwave Symp. Dig.*, pp. 969–972.

[3] N. H. Sheng, M. F. Chang, P. M. Asbeck, K. C. Wang, G. J. Sullivan, D. L. Miller, J. A. Higgins, E. Sovero, and Basit, "High power GaAlAs/GaAs HBT's for microwave applications," in *Proc. 1987 Int. Electron Device Meeting*, pp. 619–622.

[4] B. Bayraktaroglu, M. A. Katibzadeh, and R. D. Hudgens, "5 W monolithic HBT amplifier for broadband X-band applications," in *1990 IEEE Microwave and Millimeter-Wave Monolithic Circuits Symp. Dig.*, 43–45.

[5] N. L. Wang, N. H. Sheng, M. F. Chang, W. J. Ho, G. J. Sullivan, E. A. Sovero, J. A. Higgins, and P. M. Asbeck, "Ultrahigh power efficiency operation of common-emitter and common-base HBT's at 10 GHz," *IEEE Trans. Microwave Theory and Tech.*, vol. 38, pp. 1381–1389, Oct. 1990.

[6] R. C. Joy and E. S. Schlig, "Thermal Properties of very fast transistors," *IEEE Trans. Electron Devices*, vol. ED-17, pp. 586–594, Aug. 1970.

[7] S. P. Gaur, D. H. Navon, and R. W. Teerlinck, "Transistor design and thermal stability," *IEEE Trans. Electron Devices*, vol. ED-20, pp. 527–534, June 1973.

[8] P. L. Hower and V. G. K. Reddi, "Avalanche injection and second breakdown in transistors," *IEEE Trans. Electron Devices*, vol. ED-17, pp. 320–335, Apr. 1970.

[9] J. T. C. Chen and C. P. Snapp, "Bipolar microwave linear power transistor design," *IEEE Trans. Microwave Theory Tech.*, vol. MTT-27, pp. 423–430, May 1979.

[10] H. C. Poon, "Modeling of bipolar transistors using integral charge-control model with applications to third-order distortion studies," *IEEE Trans. Electron Devices*, vol. ED-19, June 1972, pp. 719–731.

[11] H. E. Abraham and R. G. Meyer, "Transistor design for low distortion at high frequencies," *IEEE Trans. Electron Devices*, vol. ED-23, pp. 1290–1297, Dec. 1976.

[12] M. E. Kim, A. K. Oki, G. M. Gorman, D. K. Umemoto, and J. B.

Camou, "GaAs heterojunction bipolar transistor device and IC technology for high-performance analog and microwave applications," *IEEE Trans. Microwave Theory Tech.*, vol. 37, pp. 1286–1303, Sept. 1989.

[13] S. I. Long, "A comparison of the GaAs MESFET and the AlGaAs/GaAs heterojunction bipolar transistor for power microwave amplification," *IEEE Trans. Electron Devices*, vol. 36, pp. 1274–1278, July 1989.

[14] R. R. Pantoja, M. J. Howes, J. R. Richardson, and C. M. Snowden, "A large-signal physical MESFET model for computer-aided design and its applications," *IEEE Trans. Microwave Theory and Tech.*, vol. 37, pp. 2039–2945, Dec. 1989.

[15] J. W. Bandler, Q.-J. Zhang, S. Ye, and S. H. Chen, "Efficient large-signal FET parameter extraction using harmonics," *IEEE Trans. Microwave Theory Tech.*, vol. 37, pp. 2099–2108, Dec. 1989.

[16] M. Weiss and D. Pavlidis, "Power optimization of GaAs implanted FET's based on large-signal modeling," *IEEE Trans. Microwave Theory Tech.*, vol. MTT-35, pp. 175–187, Feb. 1987.

[17] M. Y. Frankel and D. Pavlidis, "Large-signal modeling and study of power saturation mechanisms in heterojunction bipolar transistors," in *1991 IEEE MTT-S Int. Microwave Symp. Dig.*, pp. 127–130.

[18] S. A. Maas, *Nonlinear Microwave Circuits*, ch. 3. Norwood, MA: Artech House, 1988.

[19] V. Rizzoli and A. Neri, "State of the art and present trends in nonlinear microwave CAD techniques," *IEEE Trans. Microwave Theory Tech.*, vol. 36, pp. 343–365, Feb. 1988.

[20] Eesof: Libra™ version 2.0, 1989 by Eesof, Inc., USA.

[21] B. L. Nelson, D. K. Umemoto, C. B. Perry, R. Dixit, B. R. Allen, M. E. Kim, and A. K. Oki, "High-linearity, low dc power monolithic GaAs HBT broadband amplifiers to 11 GHz," in *IEEE 1990 Microwave and Millimeter-Wave Monolithic Circuits Symp. Dig.*, pp. 15–17.

[22] M. E. Hafizi, C. R. Crowell, and M. E. Gruppen, "The dc characteristics of GaAs/AlGaAs heterojunction bipolar transistors with application to device modeling," *IEEE Trans. Electron Devices*, vol. 37, pp. 2121–2129, Oct. 1990.

[23] J. M. Early, "Design theory of junction transistors," *Bell System Tech. J.*, vol. 32, pp. 1271–1312, Nov. 1953.

[24] R. S. Muller and T. I. Kamins, *Device Electronics for Integrated Circuits*. New York: Wiley, 1986.

[25] A. A. Grinberg, M. S. Shur, R. J. Fischer, and H. Morkoc, "An investigation of the effect of graded layers and tunneling on the performance of AlGaAs/GaAs heterojunction bipolar transistors," *IEEE Trans. Electron Devices*, vol. ED-31, Dec. 1984, pp. 1758–1765.

[26] M. R. Weiss and D. Pavlidis, "An investigation of the power characteristics and saturation mechanisms in HEMTs and MESFETs," *IEEE Trans. Electron Devices*, vol. 35, pp. 1197–1206, Aug. 1988.

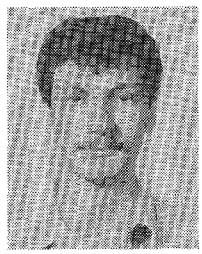

Michael Y. Frankel (S'90) was born in St. Petersburg, Russia, in 1964. He received the B.S. degree (magna cum laude) from the University of Maryland, College Park in 1986, the M.S. degree from the University of Rochester, Rochester, NY, in 1988, and the Ph.D. degree from the University of Michigan, Ann Arbor in 1991, all in electrical engineering.

He has recently joined the Naval Research Laboratory, Optical Sciences Divisions. His interests are in picosecond electronics and optoelectronics, including microwave transmission lines, photodetectors, and transistors. He has applied optoelectronic techniques to high-bandwidth transistor characterization and has developed and verified a large-signal model to analyze transistor power behavior.

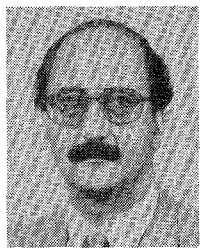

Dimitris Pavlidis (S'73—M'76—SM'83) received the B.Sc. degree in physics from the University of Patras, Greece, in 1972, and the Ph.D. degree from the University of Newcastle-upon-Tyne, U.K., in 1976. He continued as a Postdoctoral Fellow at Newcastle until 1978, engaged in work on microwave semiconductor devices and circuits.

In 1978, he joined the High Frequency Institute of the Technology University of Darmstadt, West Germany, working on III-V devices and establishing a new semiconductor technology facility. In 1980 he worked at the Central Electronic Engineering Research Institute, Pilani, India, as a UNESCO consultant. During 1980–1985, he was Engineer and Manager of the GaAs Monolithic Microwave Integrated Circuits (MMIC) Group of Thomson-CSF DHM/DAG, Corbeville, France. In this capacity, he was responsible for projects on monolithic power and broad-band amplifiers, tunable oscillators, optical preamplifiers, phase shifters attenuators, their technology and process evaluation, and the establishment of a component library for MMIC applications. He has been Professor of Electrical Engineering and Computer Science at the University of Michigan, Ann Arbor, since 1986. His current research interests cover the design and fabrication of HEMT's HBT's, strained heterostructures III-V microwave and millimeter devices and monolithic heterostructure integrated circuits.

His publications are in microwave semiconductor devices and circuits and he holds six patents on MMIC applications. In 1990 he was awarded the Microwave Prize for his work on InP Based Monolithic Integrated HEMT Amplifiers. In 1992 he was awarded the decoration of "Palmes Académiques" in the order of "Chevalier" by the French Ministry of National Education for distinguished work in the field of education.